



Differentiating Polymorphs in Molybdenum Disulfide via Electron Microscopy

Xiaoxu Zhao, Shoucong Ning, Wei Fu, Stephen J. Pennycook, and Kian Ping Loh*

The presence of rich polymorphs and stacking polytypes in molybdenum disulfide (MoS_2) endows it with a diverse range of electrical, catalytic, optical, and magnetic properties. This has stimulated a lot of interest in the unique properties associated with each polymorph. Most techniques used for polymorph identification in MoS_2 are macroscopic techniques that sample averaged properties due to their limited spatial resolution. A reliable way of differentiating the atomic structure of different polymorphs is needed in order to understand their growth dynamics and establish the correlation between structure and properties. Herein, the use of electron microscopy for identifying the atomic structures of several important polymorphs in MoS_2 , some of which are the subjects of mistaken assignment in the literature, is discussed. In particular, scanning transmission electron microscopy-annular dark field imaging has emerged as the most effective and reliable approach for identifying the different phases in MoS_2 and other 2D materials because its images can be directly correlated to the atomic structures. Examples of the identification of polymorphs grown under different conditions in molecular beam epitaxy or chemical vapor deposition, for example, 3R, 1T, 1T'-phases, and 1T'-edges, are presented, including their atomic structures, fascinating properties, growth methods, and corresponding thermodynamic stabilities.

1. Introduction

MoS_2 manifests in a wide range of polymorphs, the most common among them include semiconducting 1H- MoS_2 ,^[1–3] semimetallic 1T'- MoS_2 ,^[4–6] and metallic 1T- MoS_2 ,^[7,8] in which their different intralayer stacking order, that is, how the S layer

is stacked with respect to the Mo layer in one unit cell, makes them structurally distinct (Figure 1a). The intralayer stacking sequence also determines the splitting of degenerate d bands, leading to a different progressive filling of nonbonding d bands, and thus distinct electronic properties.^[9,10] Adding to these is another degree of freedom by adopting different interlayer stacking sequences between individual S-Mo-S layers in multilayer MoS_2 . Multilayer 1H phase MoS_2 exhibits a variety of stacking polytypes, such as 2H and 3R when the interlayer stacking orders follow the AA' and ABC sequence, respectively (Figure 1b). Note that bilayer 3R-stacked MoS_2 shows the AB stacking sequence, whereas trilayer follows the ABC sequence. Unlike 2H, 3R- MoS_2 does not have inversion symmetry, thus 3R can be distinguished from 2H by second harmonic generation.^[11,12] Despite theoretical predictions of unique properties in the 1T and 1T' polymorphs such as ferromagnetism,^[13] Weyl semimetallicity,^[14] and superconductivity,^[15] the realization of these properties is hampered by the considerable difficulty to grow macroscopically large MoS_2 crystals of polymorphs other than the prevalent H phase. The metastability of the 1T and 1T' phases also mean they degrade rapidly under ambient conditions,^[4] making their identification challenging. Differentiating the various polymorphs is the first step to understand the structure-dependent properties of MoS_2 . With the advent of the spherical aberration corrector and cold field emission gun,^[16,17] the spatial resolution of conventional transmission electron microscopy (TEM) and scanning TEM (STEM) at low accelerating voltage has reached the sub-angstrom level in recent years.^[17] The collected STEM-annular dark field (ADF) integrated intensity for one atom column oriented along the electron beam direction varies with atomic number Z as $\approx Z^{1.67}$,^[16] and for monolayer and bilayer materials it is also approximately linear with the number of atoms contained in a column. Therefore, the atom packing information along the z-axis of a specific stacking polytype in few-layer MoS_2 is intimately tied to its STEM image contrast,^[18] making STEM a powerful characterization tool for investigating the polymorphs and stacking polytypes in mono- and multilayer MoS_2 films.^[2,6,12]

Here, we discuss recent progress made on the growth and identification of various polymorphs of MoS_2 . The advantages of employing STEM-ADF for the phase identification of

X. X. Zhao, Dr. W. Fu, Prof. K. P. Loh
Department of Chemistry
National University of Singapore
3 Science Drive 3, Singapore 117543, Singapore
E-mail: chmlohp@nus.edu.sg

X. X. Zhao, Prof. S. J. Pennycook, Prof. K. P. Loh
NUS Graduate School for Integrative Sciences and Engineering
National University of Singapore
13 Centre for Life Sciences, #05-01, 28 Medical Drive
Singapore 117456, Singapore

Dr. S. C. Ning, Prof. S. J. Pennycook
Department of Materials Science and Engineering
National University of Singapore
9 Engineering Drive 1, Singapore 117575, Singapore

The ORCID identification number(s) for the author(s) of this article can be found under <https://doi.org/10.1002/adma.201802397>.

DOI: 10.1002/adma.201802397

mono- and few-layer MoS₂ are presented, with emphasis on the pitfalls to avoid.

2. Identification of MoS₂ Polymorphs and Stacking Polytypes by Aberration-Corrected STEM

2.1. Atomic Structures of Various Polymorphs in MoS₂

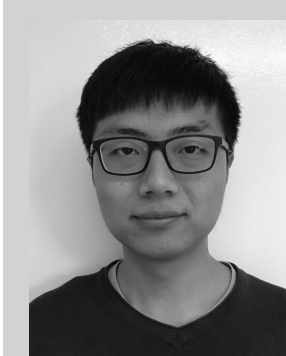
In monolayer 1H and 1T-phase MoS₂ (Figure 2a,b), each individual layer consists of three atomic planes (S-Mo-S), the top and bottom planes being sulfur atom planes with P_{6m} wallpaper group symmetry, with the sandwiched Mo atom plane sharing the same planar symmetry.^[9,10] The intralayer stacking order in 1H-MoS₂ and 1T-MoS₂ takes AbA and AbC stacking sequences, respectively. 1T-MoS₂ is dynamically unstable, and it undergoes a Peierls distortion to reduce the dimensionality of the 2D system into three equivalent 1D zigzag (ZZ) chains, giving rise to the so-called distorted 1T phase (Figure 2c), denoted as 1T' or ZT phase.^[4,6] Various stacking polytypes have been documented in multilayer H-phase MoS₂, such as 2H and 3R (Figure 2d-f), which follows the AA', AB, or ABC sequences, respectively.^[9,10] Note that the prime symbol represents the mirror symmetry. Few reports have discussed the stacking polytypes induced by the stacking of 1T or 1T' phases, presumably due to their poor stability.^[7]

2.2. Polymorph Identification via High-Resolution TEM (HRTEM) and Selected Area Electron Diffraction (SAED)

HRTEM and SAED images are both acquired with a parallel incident electron beam. The HRTEM image, or the phase contrast image, is recorded from the real space intensity of the electron wave modulated by the sample and microscope objective lens. Its real space contrast varies when sample thickness and objective lens aberrations such as defocus and spherical aberration change.^[19] Therefore, the bright and dark blobs in the HRTEM images of MoS₂ are sometimes mistaken for atom columns and interstices, respectively.^[20] Although the sample structure could be deciphered via multislice simulation^[21] or exit wave reconstruction,^[22,23] the high time consumption of this technique limits its application in static structure analysis. SAED records the far field electron intensity diffracted from the region with dimensions in the range of hundreds of nanometers, and it could be approximated as the squared magnitude of the Fourier transform of the electron exit wave function.^[24] More direct structure information could be acquired via SAED compared to HRTEM due to the elimination of the objective lens transfer function but at the sacrifice of spatial resolution. However, the Bragg peak intensities are modulated not just by lattice spacing but also by the surface profiles of the material,^[25,26] which increases the difficulties in differentiating polymorphs in 2D materials via HRTEM and SAED.^[20,27]

2.3. Polymorph Identification via STEM-ADF

The STEM-ADF imaging technique utilizes the converged electron beam to reveal the localized atomic structure.^[28] The



Xiaoxu Zhao is a doctoral candidate in the Graduate School for Integrative Sciences and Engineering at the National University of Singapore. He received his B.Eng. degree from the School of Materials Science and Engineering at Nanyang Technological University, Singapore, in 2014. His research focuses on the scanning transmission electron microscopy/electron energy-loss spectroscopy analysis of 2D materials and single atom catalysis.



Stephen J. Pennycook is a professor in the Materials Science and Engineering Department, National University of Singapore (NUS), an adjunct professor at the University of Tennessee, and adjoint professor in Vanderbilt University, USA. Previously, he was corporate fellow in the Materials Science and Technology Division of Oak Ridge National Laboratory and leader of the Scanning Transmission Electron Microscopy Group. He joined NUS in 2015.



Kian Ping Loh is currently Provost's chair professor in the Department of Chemistry, National University of Singapore, and head of the 2D materials group in the Centre for Advanced 2D Materials. His research interests are focused on the growth, applications and interesting physics of 2D materials.

integration of elastic and inelastic scattered electrons on the STEM-ADF detector cancels the transverse and longitudinal coherency of the electron beam.^[29] The contrast of STEM-ADF is named as incoherent Z contrast,^[30,31] in which elemental and structural information can be revealed simultaneously. Therefore, the Z-atom information of MoS₂ can be directly translated into the contrast in STEM-ADF images, making it a powerful characterization tool for uncovering the structure of 2D materials. In addition, varying the defocus value of the objective lens to converge the electron beam at different depths, localized 3D information on material structure can be potentially resolved via 3D depth sectioning.^[32]

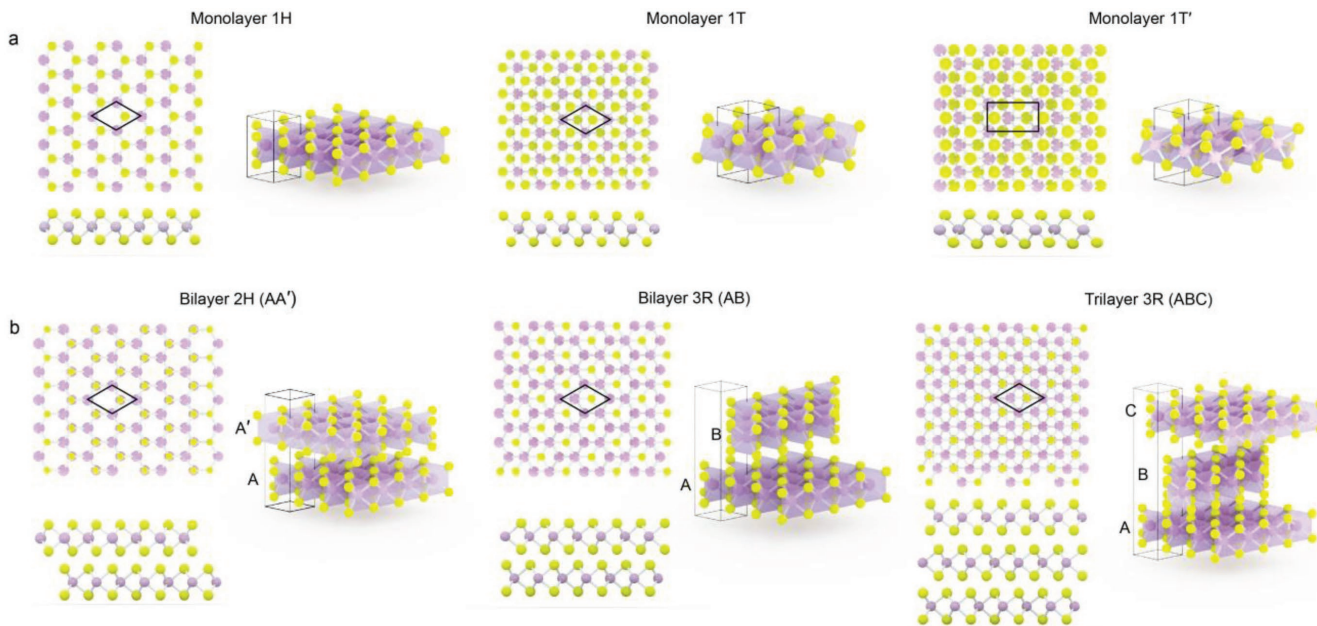


Figure 1. Atomic structures of various polymorphs in MoS₂. Atomic models of: a) monolayer 1H, 1T, 1T', and b) bilayer 2H, 3R, and trilayer 3R-stacked MoS₂, respectively. The side views and perspective views are depicted in the lower and right panels, respectively.^[10]

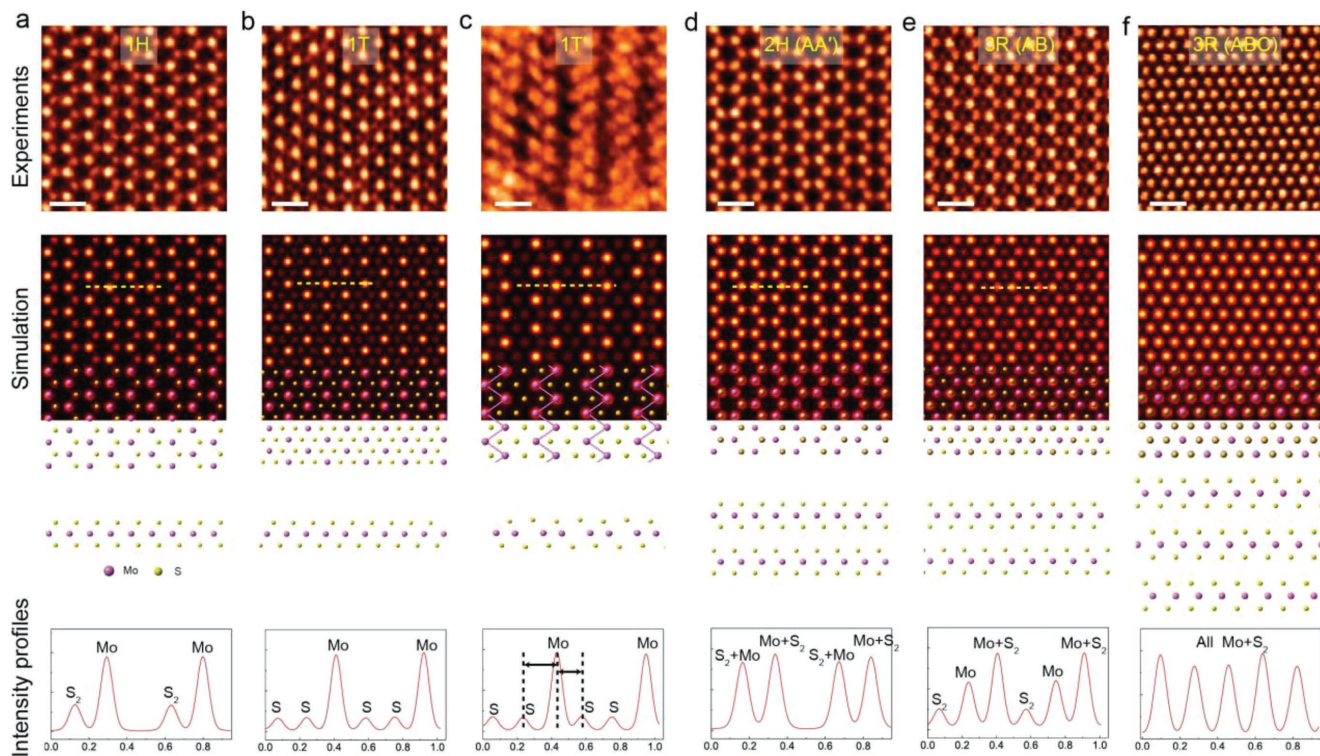


Figure 2. Atomic-resolution STEM-ADF images of monolayer: a) 1H, b) 1T, c) 1T', d) bilayer 2H (AA'), e) bilayer 3R (AB)-stacked, and f) trilayer 3R (ABC)-stacked MoS₂. Corresponding simulation results overlaid with atomic models are displayed in the lower panels. The intensity line profiles of each atomic model from the yellow dashed lines are depicted below. The unit is nm in all line profiles. The digits stand for the number of MoS₂ layers in the unit cell, and the letters indicate the crystal family where H stands for hexagonal, T stands for trigonal, and R stands for rhombohedral, respectively. Note that bilayer 3R represents the AB stacking order. Scale bars: 0.5 nm. a) Adapted with permission.^[55] Copyright 2016, Wiley-VCH. b) Adapted with permission.^[26] Copyright 2016, American Chemical Society. c) Adapted with permission.^[6] Copyright 2016, American Chemical Society. d-f) Adapted with permission.^[12] Copyright 2018, Wiley-VCH.

2.4. Applications to Phase Identification of MoS₂

Monolayer 1T- and 1H-MoS₂ can be directly distinguished by the intensity of sulfur atom columns in the STEM-ADF image. In Figure 2a,b, experimental and simulated STEM-ADF images of both phases are shown, and the corresponding atom columns are marked. Due to the overlap of the two sulfur atoms in the 1H phase along the beam direction, the intensity of the atom column containing the S dimer in the simulated 1H phase image is doubled compared to that in 1T phase image as verified by the intensity line profiles. It is often difficult to resolve single sulfur atoms in the 1T phase^[33] due to surface contamination, and/or a nonlinear relationship between the image intensity and number of collected electrons, particularly when a high contrast is employed for visualizing 2D materials.^[34] To enhance the contrast of the S monolayers in 1T-MoS₂, a lower accelerating voltage and use of the medium angle annular dark field (MAADF) detector for imaging is recommended.

In the 1H phase, two layers of sulfur form an eclipsed configuration and the atom column contains two S atoms which form a dimer-like structure, which can be easily seen by STEM. This contrasts with the staggered configuration of the two S atoms in the 1T phase, each atom column containing one sulfur atom which can hardly be seen by STEM.^[26,33,35] In multilayer films however, the presence of “stacking polytypes” complicates the polymorph identification. This is because the STEM image is basically a projected 2D image from a 3D structure. For example, the bilayer AA-stacked 1T film shares exactly the same STEM image as a bilayer AB'-stacked 1H film.^[36]

A STEM-ADF image of the 1T'-MoS₂ phase shows distinctive Mo zigzag chains (Figure 2c) where periodic in-plane S-S contraction and elongation is found, as shown in the intensity line profile. In addition, (2 × 1) superspots appear in the corresponding fast Fourier transform (FFT) pattern regardless of the sample thickness. Although bilayer 2H-MoS₂ (Figure 2d) and monolayer 1H-MoS₂ (Figure 2a) share similar projected atomic structure, the intensity of Mo and S₂ atom blobs in the honeycomb of 1H-MoS₂ (Figure 2a) reveals a discernible intensity variation while the corresponding intensity variations of Mo+S₂ and S₂+Mo atom blobs in bilayer-MoS₂ (Figure 2d) are quite similar. Bilayer 3R-stacked MoS₂ (Figure 2e) can be distinguished by the appearance of weak spots in the center of each hexagon, compared to 2H.^[12,37] Although there are similarities between the projected atomic patterns of 1T-MoS₂ and bilayer 3R-MoS₂, the intensity of the three atom column spots in bilayer 3R-MoS₂ are well resolved. For example, the intensities of Mo+S₂, Mo, and S₂ atom blobs in each unit cell reveal a decreasing contrast, whereas the contrast of the two S monomers in the 1T phase is equal and much weaker than that of the Mo atom, hence could be easily buried in the background intensity (Figure 2d,e). In trilayer 3R-MoS₂ all atom columns contain an equivalent number of atoms, that is, Mo+S₂, therefore no discernible contrast variations could be found in trilayer 3R-MoS₂ among all atom blobs (Figure 2f).

2.5. Commonly Encountered Challenges in STEM-ADF Analysis

In this section, we will discuss the commonly encountered challenges on phase differentiation of MoS₂ via STEM-ADF imaging.

2.5.1. STEM-ADF Imaging with Low Signal-to-Noise (S/N) Ratio

The S/N ratio of the STEM image can be degraded by random Poisson noise^[38] and scanning noise^[39] during the image capture. In addition, surface contamination^[40] as well as any underlying thin carbon film^[41] reduce the S/N ratio. In many reports, the assignment of 1T-MoS₂ has been made on the basis of the absence of the S dimer, however, the S dimer in 1H-MoS₂ is sometimes obscured by contamination^[12] or an underlying carbon film. Therefore, to differentiate the 1T and 1H phase in a noisy STEM-ADF image is challenging.

2.5.2. Influence of Improper Filtering

To enhance the image S/N ratio and fidelity in structural analysis, many post image processing techniques have been employed. However, when filters such as a Fourier filter are applied to experimental data with low S/N ratio (Figure 3a), artifacts such as pseudo atom column blobs (Figure 3b) can appear in the 1H-MoS₂ structure. Also, the Fourier filtered image may not reliably represent the real atomic structure due to lens astigmatism and other residual aberrations. As shown in Figure 3d, the intensity profile marked by the red line in the Fourier filtered image (Figure 3b) based on the STEM image of a noisy 1H-MoS₂ (Figure 3a) shows the appearance of pseudo atom columns, which can be wrongly interpreted as the 1T phase. The phases and amplitudes of the Bragg peaks in the frequency space of experimental images can deviate from those of pristine samples due to surface contamination and lens aberrations.^[42] In fragile 2D samples, the periodicity can be interrupted by surface ripples and morphology changes induced by the high energy electron beam.^[43]

In the experimental STEM-ADF image, the periodicity in the image may be interrupted by lattice distortion and phase boundaries.^[25,44–46] Fourier filtering will modify the actual structure information, especially along boundaries or edges. The information containing the exact boundary configuration exists in the region between Bragg peaks, therefore, structural information derived from MoS₂ boundaries, edges, or islands^[47] after filtering may considerably deviate from the actual information and is not recommended for phase identification.

2.5.3. Other Challenges

The theoretical lattice parameters of 1T and 1H-MoS₂ differ from each other by <0.01 Å,^[4,5,48] and such small differences are obscured by scanning noise, local lattice distortion, rippling effects, etc. Therefore, the phase identification of 1T-MoS₂ by determining the lattice constant is not reliable.^[49] In the literature, rotational disorder^[49] and bilayer 3R-stacked MoS₂^[27] have sometimes been misassigned as 1T-MoS₂. In addition, when the orientation of the MoS₂ film deviates from the exact [0001] zone axis, as is common along the edge regions, 1T-phase identification becomes much more challenging and additional image simulations need to be conducted.

Therefore, the identification of 1T-MoS₂ is not without pitfall. We have listed a few challenging situations below that may

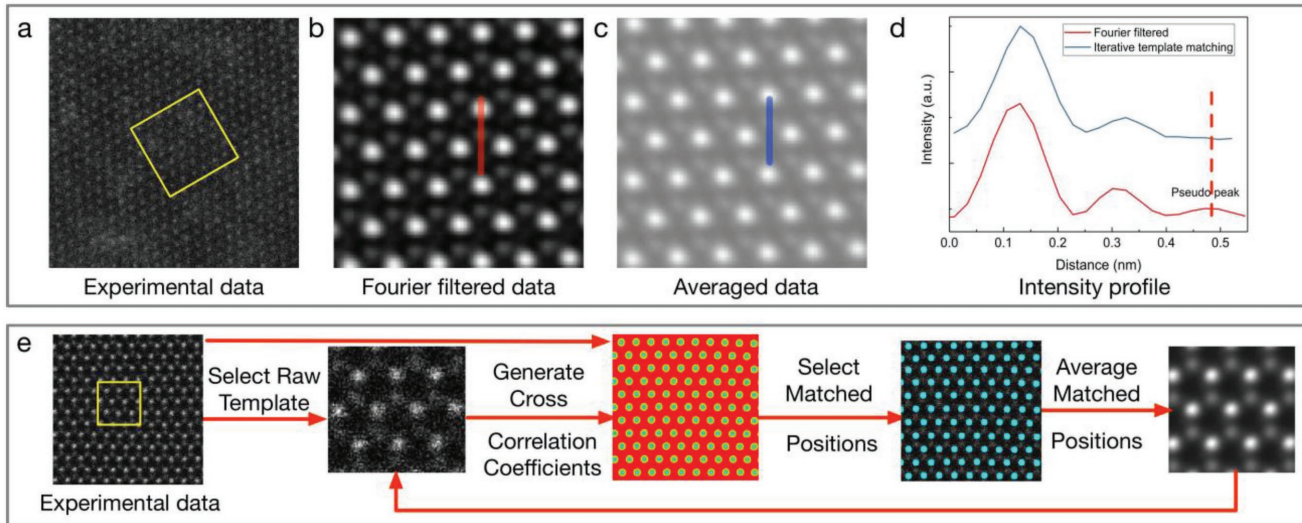


Figure 3. Iterative template matching methods. a) A typical STEM-ADF image of surface contaminated CVD grown monolayer 1H-MoS₂ film. b) The Fourier filtered image of the yellow box region in (a). c) Iterative template matching processed image of the same region in (a). d) Intensity line profiles of the red line in (b), and blue line in (c). Pseudo peaks are observed in the Fourier filtered image but avoided by template matching. e) Flow chart of the iterative template methods for enhancing the S/N ratio of a 1H-MoS₂ image.^[51] a,b) Adapted with permission.^[12] Copyright 2018, Wiley-VCH.

lead to wrong interpretation: (1) Noisy 1H-MoS₂ images, (2) Fourier filtering a noisy 1H-MoS₂ image, (3) phase differentiation based on 1H/1T lattice mismatch,^[49] (4) bilayer 3R-stacked MoS₂,^[27] (5) 1T'-MoS₂,^[50] and (6) twisted bilayer or few-layer MoS₂.^[49]

2.6. Recommended Image Processing Method for Phase Identification

A real space method based on template matching^[51] is recommended to generate an averaged structure with enhanced S/N ratio. Figure 3e shows the workflow; first, the STEM-ADF image should be low-pass filtered, to remove frequencies above the information limit of the microscope. Then the influence of the scanning noise will be suppressed, but the sample spatial frequencies are retained. Next, an arbitrary region (Figure 3e), larger than the size of the unit cell, serves as the starting template for the averaged structure.^[51] After the cross-correlation coefficients are computed with the template using the whole frame, the maxima of these coefficients accurately correspond to the positions of matched regions. Finally, the template is updated each time by averaging the matched regions, and the above procedure can be repeated iteratively to enhance the S/N ratio as indicated by the red arrows.^[52] In Figure 3c, an averaged region of a contaminated 1H-MoS₂ image (Figure 3a) is generated via the above iterative template matching method. As shown by its line profile in Figure 3d marked by the blue line, the pseudo atom blobs induced by Fourier filtering are eliminated confirming the 1H phase of MoS₂. In addition, a strong background due to the surface contamination is retained. While this method is reliable for phase identification, one drawback is that it will average out any point defects.

3. Stacking Polytypes in Multilayer H-Phase MoS₂

Geometrically there are five different types of stacking polytypes in bilayer H-phase MoS₂ films,^[53] and 15 types^[36] in three-layer films if staggered and eclipsed configurations are considered solely. So far, only 2H^[54,55] and 3R^[12,56] stacking polytypes have successfully been fabricated in large scale. Other stacking orders, such as AA, A'B, and AB' are rarely reported.^[36,53,57] In addition, few reports have discussed the stacking polytypes induced by stacking of the T or T' phase, attributed presumably to their poor stability.^[7]

Bulk 3R crystals assume a periodic ABC stacking order, and bilayer 3R phase takes the AB stacking sequence. The presence of broken inversion symmetry in monolayer 1H-MoS₂ affords its wide applications in nonlinear optics,^[56] and valleytronics.^[11,57] Those fascinating properties, however, vanish in even-layered 2H-stacked MoS₂ films due to the recovery of centrosymmetry.^[11] In 3R-stacked MoS₂ however, each layer shares the same crystallographic orientation and shifts relative to the bottom layer by $\frac{\sqrt{3}}{3} a$ along the ZZ direction, leading to a staggered ABC stacking order.^[53,57] This staggered stacking geometry maintains non-centrosymmetry regardless of the layer number. Thus, 3R-MoS₂ films show enhanced nonlinear response and robust spin polarization.^[56]

The 3R-stacked MoS₂^[36] however is less thermodynamically favorable as compared to 2H-stacked MoS₂, thus synthetic MoS₂ crystals predominantly adopt the 2H stacking registry.^[55] Recently,^[12] we successfully grew dendritic structures of 3R-stacked bilayer MoS₂ under a nonequilibrium chemical vapor deposition (CVD) growth condition.^[58] Exploiting the inherent microscopic anisotropy of transition metal dichalcogenide (TMD) crystals, the growth rate anisotropy of the Mo and S edges is especially accentuated at low S chemical potentials,

leading to the growth of highly organized MoS₂ dendrites which are 3R-stacked. One consistent trend is that a high growth temperature (≈ 1050 °C) favors the growth of 3R-stacked MoS₂ crystals.^[12] The presence of 3R stacking registry is confirmed by atomic-resolution STEM-ADF imaging (Figure 4a), where weak atom blobs are formed in each honeycomb as shown in the enlarged image (Figure 4b). In addition, the intensity ratio between the three unique atom columns, that is, Mo+S₂, Mo, and S₂, in bilayer 3R-stacked MoS₂ match perfectly with the simulation results (Figure 4c,d). The exposed edges are assigned to Mo-ZZ edges (Figure 4e,f) according to the interlayer stacking order. The large-scale formation of bilayer 3R-stacked MoS₂ films was further verified by the giant enhancement of second and third harmonic generation (SHG and THG) (Figure 4g,h). The transformation from 2H to 3R stacking polytypes in bilayer MoS₂ films can be accomplished by introducing

a mirror symmetry operation plus a relative in-plane displacement.^[36,59] For example, we found that the presence of a mirror twin boundary (MTB) could accommodate the formation of 2H|3R lateral hybrid structures (Figure 4i,j) in various bilayer group VIB TMD films (MoS₂, MoSe₂, and WSe₂). Interestingly, when two MTBs in two different layers are within interaction distance, a lateral 3R|2H|3R lateral hybrid structure (Figure 4k,l) is formed. The size of the 2H domains increases linearly with the separation distance between the two MTBs.^[53] Recently, Wu and co-workers^[60] found that introducing Nb substitution into MoS₂ crystals leads to the formation of 3R-stacked MoS₂ crystals. Density functional theory (DFT) calculation suggests that the 3R-stacked MoS₂ becomes thermodynamically stable in the presence of Nb dopants and overtakes 2H as the most thermodynamically stable stacking order when the Nb doping level exceeds 1.4%. Cortes et al.^[61] found that

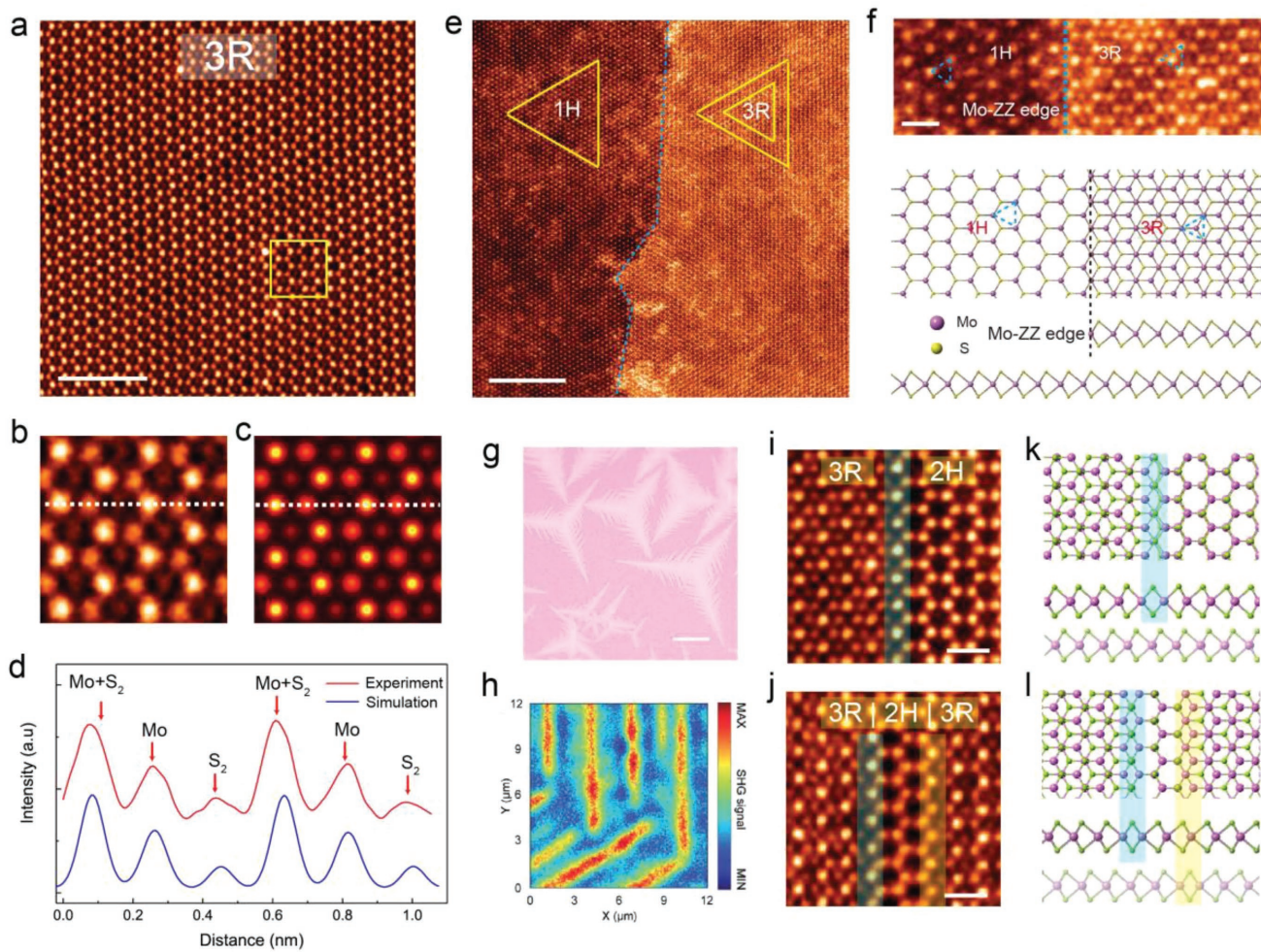


Figure 4. Controlled growth of bilayer 3R-stacked MoS₂ films. a) Atomic-resolution STEM-ADF image of a bilayer 3R-stacked MoS₂ film. b) The enlarged yellow box region from (a), and c) the corresponding simulated image. d) Intensity line profiles from the white dashed lines in (b) and (c) showing the intensity variations in bilayer 3R-stacked MoS₂ films. e) A STEM-ADF image showing a mono- and bilayer MoS₂ film, with the bilayer region exhibiting a 3R (AB) stacking registry. f) Atomic-resolution STEM-ADF image depicting the 1H to 3R transition across the interface; the exposed edges are Mo-ZZ edges. The atomic models are shown in the lower panel. g) Optical image of dendritic-like MoS₂ crystals. h) Nonlinear spectral images acquired at the corresponding SHG and THG emission wavelengths. i,j) Atomic-resolution STEM-ADF images of bilayer MoSe₂-1 MTB (i) and bilayer MoSe₂-2 MTB (j) films revealing 3R|2H and 3R|2H|3R lateral hybrid structures. k,l) Atomic models of bilayer MoSe₂-1 MTB (k) and bilayer MoSe₂-2 MTB (l) films are displayed in the lower panels. MTBs are highlighted by cyan and yellow false color. Scale bars: 2 nm in (a), 5 nm in (e), 0.5 nm in (f,i,j), and 100 μm in (g). a-h) Adapted with permission.^[12] Copyright 2018, Wiley-VCH. i-l) Reproduced with permission.^[53] Copyright 2018, American Chemical Society.

Mo interstitials stabilize the 3R phase, which suggests that the phase conversion can be controlled by increasing the chemical potential of Mo during growth. In addition, 3R-stacked MoS₂ had also been prepared by artificial folding of monolayer films, and several other stacking polytypes have successfully been realized.^[57] It is worth pointing out that 3R-stacked MoS₂ films have been reported to show enhanced hydrogen evolution reactivity compared to 2H-stacked MoS₂ films.^[37]

4. Polymorphs in Monolayer MoS₂

4.1. 1T Phase

The 1T phase is one of the most widely encountered polymorphs in MoS₂. It is metallic, unlike the semiconducting 1H-MoS₂, which favors applications in catalysis and energy storage. In stark contrast to air stable semiconducting H-phase MoS₂, 1T-MoS₂ is dynamically unstable.^[4,6,48] Due to the huge energy barrier of 0.85 eV/unit cell for the transition from 1H to 1T phase,^[4,5] direct growth of 1T-MoS₂ by CVD or molecular beam epitaxy (MBE) at high temperature is difficult. Recently, Chen and co-workers^[26,33,62] reported the direct growth of 1T-MoS₂ (Figure 5a,b) and alloyed 1T-Mo_{1-x}W_xS₂ by CVD (Figure 5c). The formation of the 1T phase is believed to be associated with the in-plane thermal strains imposed by the substrate, which permits the phase transformation from 1H to 1T during the cooling process.^[33] When the 1T and 1H phases meet at the domain boundary, atomically sharp 1T|1H junctions

(Figure 5a) are formed,^[26] suggesting that devices based on lateral heterophases can be made into metallic-semiconductor-type junctions.^[7] The phase transition from 1T to 1H is further confirmed by the intensity line profile (Figure 5b) where the intensity of staggered S monomers in the 1T phase is almost half that of the eclipsed S dimer in the 1H phase. Solvothermal synthesis is another approach for synthesizing 1T-MoS₂.^[63] However, instead of the 1T phase, electron microscopy data shown in the reports indicate the presence of 1T' phase, which can be judged by the presence of zigzag chains in the atomic-resolution STEM images or the appearance of superspots in the SAED or FFT patterns.^[6,64] It is quite rare to find the 1T phase in solution phase synthesized flakes,^[27,65] perhaps due to the rapid phase transformation from the 1T to 1T' phase.

Other than direct growth, a variety of post phase transformation methods have been developed to prepare the 1T phase, and these have relied on charge transfer to stabilize the metastable 1T phase. Electron beams (Figure 5d,e),^[35] alkali metals,^[7] donor element dopants,^[66] and electrostatic gating^[67] have also been demonstrated as effective approaches for realizing the 1H to 1T phase transformation.

4.2. Structure and Properties of 1T'

1T'-MoS₂ is semimetallic and exhibits a small direct bandgap of about 22 meV.^[4,5] DFT calculations show that it is more stable than 1T-MoS₂ but less stable than 1H-MoS₂.^[4,48] The 1T' phase can be considered as a charge density wave state of

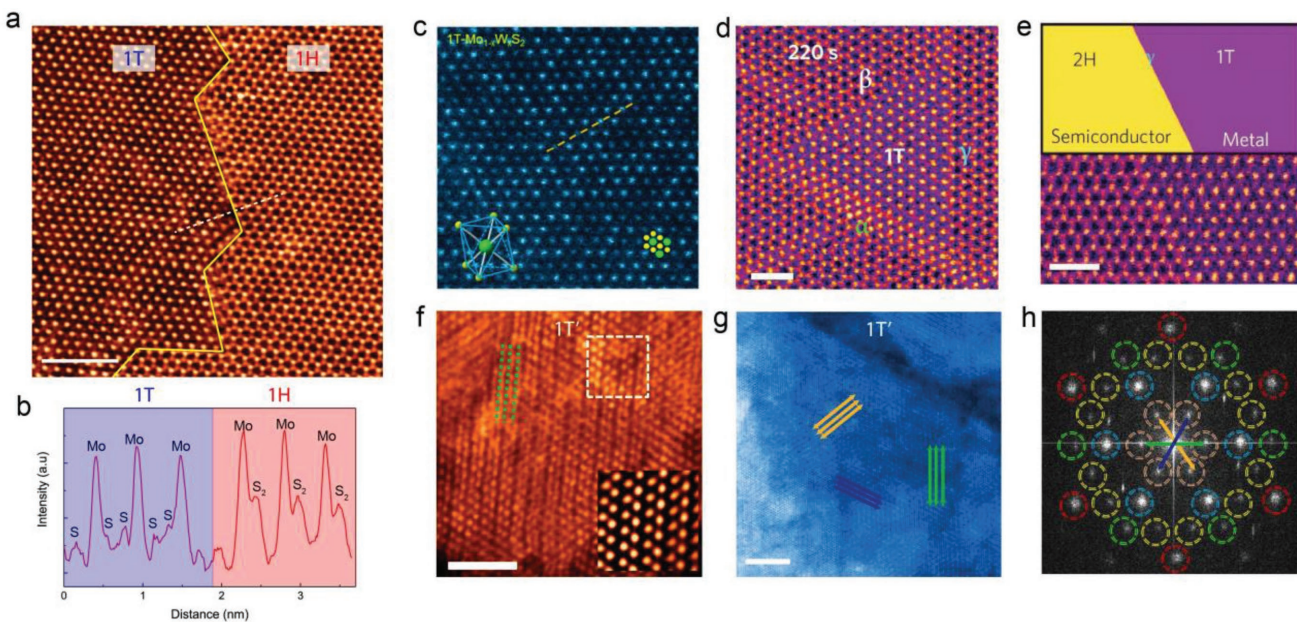


Figure 5. Synthesis of 1T and 1T'-MoS₂. a) An atomic-resolution STEM-ADF image of an atomically thin phase boundary (indicated by the arrows) between the 1T and 1H phases in a monolayer MoS₂ film. b) Intensity line profile of the white dashed line in (a) confirming the 1T/1H phase boundary. c) STEM-ADF image of the CVD-grown Mo_{1-x}W_xS₂. d,e) STEM-ADF image of electron beam irradiation induced 1H and 1T heterostructure in a monolayer MoS₂ film. f) An atomic-resolution STEM-ADF image of a typical grain orientation with inset showing a filtered magnified image of the degenerate 1D zigzag chains. g) A typical STEM-ADF image of 1T'-phase Li_xMoS₂ and h) the corresponding FFT pattern with three orientation variants highlighted by yellow, blue, and green arrows. h) An atomic-resolution STEM-ADF image of a typical grain orientation with inset showing a filtered magnified image of the degenerate 1D zigzag chains. Scale bars: 2 nm in (a,f), 1 nm in (d,e), and 5 nm in (g). a,b) Adapted with permission.^[26] Copyright 2016, American Chemical Society. c) Reproduced with permission.^[33] Copyright 2018, American Chemical Society. d,e) Reproduced with permission.^[35] Copyright 2014, Nature Publishing Group. f-h) Reproduced with permission.^[6] Copyright 2016, American Chemical Society.

1T-MoS₂ due to the Peierls instability, which manifests as a (2 × 1) superstructure. Due to the unique quasi-1D array structure, 1T'-MoS₂ shows peculiar properties like the quantum spin Hall effect,^[68] Weyl semimetallicity,^[14] dipolar ferroelectricity,^[69] superconductivity,^[15] charge density wave formation,^[70] and nonlinear optical properties.^[71] In addition to 1T', other forms of distorted 1T phase, denoted as 1T'' or DT, have been predicted by theory. The 1T'' phase reveals a 2 × 2 superstructure (tetramerization) and it exhibits supreme electron (hole) mobility comparable to that of graphene.^[4] However, the atomic structure of 1T''-MoS₂ has rarely been reported. So far nanosized 1T''-MoS₂ domains have been observed in chemically exfoliated nanosheets,^[48] and nanosized 1T''-WS₂ domains have been produced in situ and characterized by e-beam irradiation in STEM.^[72]

The preparation of 1T'-MoS₂ was first demonstrated in 1992 by Wypych et al.^[73] via the sulfidation of K₂MoO₄ to form an intermediate 1T' phase K_{1-x}(H₂O)_yMoS₂, as confirmed by SAED^[74] and scanning tunneling microscopy (STM).^[75] Subsequently, the intercalated K was removed in water, leading to

the formation of large-scale high-quality 1T'-MoS₂ crystals.^[64,76] It should be noted that the 1T' phase was commonly misassigned as "1T" in these papers. The 1T'-MoS₂ crystals prepared by sulfidation of K₂MoO₄ are not thermodynamically stable and are convertible to 2H-MoS₂ following thermal annealing (<100 °C) or laser irradiation.^[77] So far, the preparation of 1T'-MoS₂ is predominantly realized via 1H to 1T' phase transformation, similar to the fabrication of the 1T phase. Alkali metal intercalation is usually applied to trigger the phase evolution.^[15] In our recent report,^[6] we used lithium naphthalenide and achieved nearly 100% 1T'-MoS₂ conversion (Figure 5f). The synthesized 1T'-MoS₂ sheets consist of mosaic-like 1T' nanocrystalline domains (Figure 5g,h), which enable a much higher cycle stability, capacity, and rate capability compared to polycrystalline MoS₂ flakes when utilized as the electrode for lithium-ion batteries.^[6] The 1T' phase can also be produced by solid-phase reaction between bulk MoS₂ crystals and thermally evaporated lithium;^[71] lithiated 1T'-phase MoS₂ affords giant optical Kerr nonlinearity and high optical transparency. It should be noted that again a few reports^[50,63,73,75,76] mistakenly assigned the 1T'

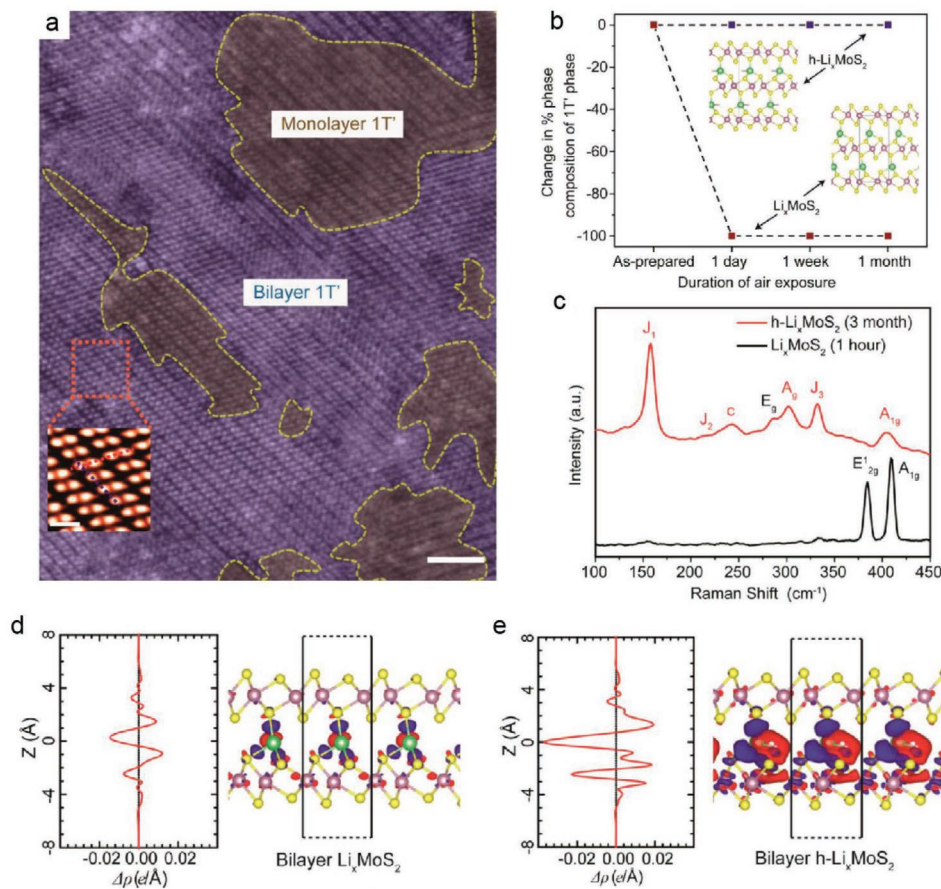


Figure 6. Stabilization of 1T'-MoS₂ via hydrogenation. a) STEM-ADF image showing monolayer and bilayer h-Li_xMoS₂ regions with false color to differentiate the different layers. The inset shows a magnified filtered image of the 1T' phase region in the dotted orange box. b) Degradation of h-Li_xMoS₂ in ambient conditions, investigated by the change in % 1T' phase compositions as determined by XPS. c) Raman spectra of h-Li_xMoS₂ and Li_xMoS₂. Duration of air exposure is indicated in brackets next to their label. Raman modes unique to the 1T' phase are labeled in red. d,e) DFT-calculated differential charge density after intercalation of Li (d) and LiH (e) into bilayer 1T'-MoS₂. Plane-averaged differential charge density ($\Delta\rho(z)$) plots are shown in the left panels of the region marked by a black box of the isosurface side-view profiles at 0.02 Å⁻³ in the right panels. The black dashed lines refer to an interface with vacuum. The red (blue) color of the isosurface plots denotes loss (accumulation) of electrons in the system. Scale bars for the image and inset are 2.5 nm and 0.5 nm, respectively. a–e) Reproduced with permission.^[71] Copyright 2017, American Chemical Society.

phase as 1T phase in their alkaline metal intercalated MoS₂ films.

Due to its metastability, there is a need to identify a robust method to stabilize the 1T' phase. We found that hydrogenation of lithium intercalated 1T'-MoS₂ is an efficient and robust method to stabilize 1T'-MoS₂ (Figure 6a) due to the formation of a relatively stable lithium hydride ($\text{h-Li}_x\text{MoS}_2$) phase compared to the highly reactive lithium. The spectroscopic signatures of 1T' phase in hydrogenated 1T'-MoS₂, as tracked by X-ray photoelectron spectroscopy (XPS), Raman spectroscopy (Figure 6b,c), and X-ray diffraction (XRD), remain stable for over a month. The increased stability of the 1T' phase in LiH-intercalated MoS₂ is due to two reasons. First, the formation of lithium hydride passivates the Li from reacting with air. Second, LiH (0.879 e/lithium atom) acts as a strong electron donor to MoS₂, and stabilizes the 1T' phase (Figure 6d,e). DFT calculations also reveal a significant charge redistribution induced by the relatively large dipole moment of LiH, especially in between the MoS₂ layers, as shown by the isosurface plots in Figure 6d,e. The increase in dipole–dipole interactions creates a strong intermolecular force which decreases the chemical energy of the system. Importantly, it was found that the hydrogenation of the alkali metal intercalant to form alkali metal hydrides, for example, potassium hydride, sodium hydride, and

lithium hydride, improve the air-stability of the respective 1T' phases significantly over pure alkali metal intercalants.^[71]

Although it is difficult to grow the 1T' phase as a film directly due to its metastability, we find that it may exist as a 1D structure at edges or domain discontinuities. STEM revealed that the edges of nanoporous H-phase MoS₂ films grown by MBE under Mo-rich (high Mo flux) conditions are 1T'-like (Figure 7a).^[78] The as-grown 1T'-edges remain stable at 900 °C as confirmed by in situ STEM experiments (Figure 7b,c). In the 1T' edges, the outermost atoms are made of a strip of Mo atoms, and the sulfur dimers split into a staggered configuration, similar to that in the 1T-phase.^[9] The experimentally observed atomic structure was further verified by combined DFT calculation and image simulation (Figure 7d). Analyzing nanoporous MoS₂ films by STEM, we found that the 1T' phase can be grown and stabilized at the edges while the basal plane is comprised of the 1H phase. In addition to 1T' edges, Mo-Klein edges (Figure 7e), S-ZZ edges (Figure 7f), and Mo-ZZ (Figure 7g) edges were also identified.^[79]

5. Conclusions and Outlook

The synthesis of large-area MoS₂ polymorphs other than the thermodynamically stable 2H phase is a challenging task.

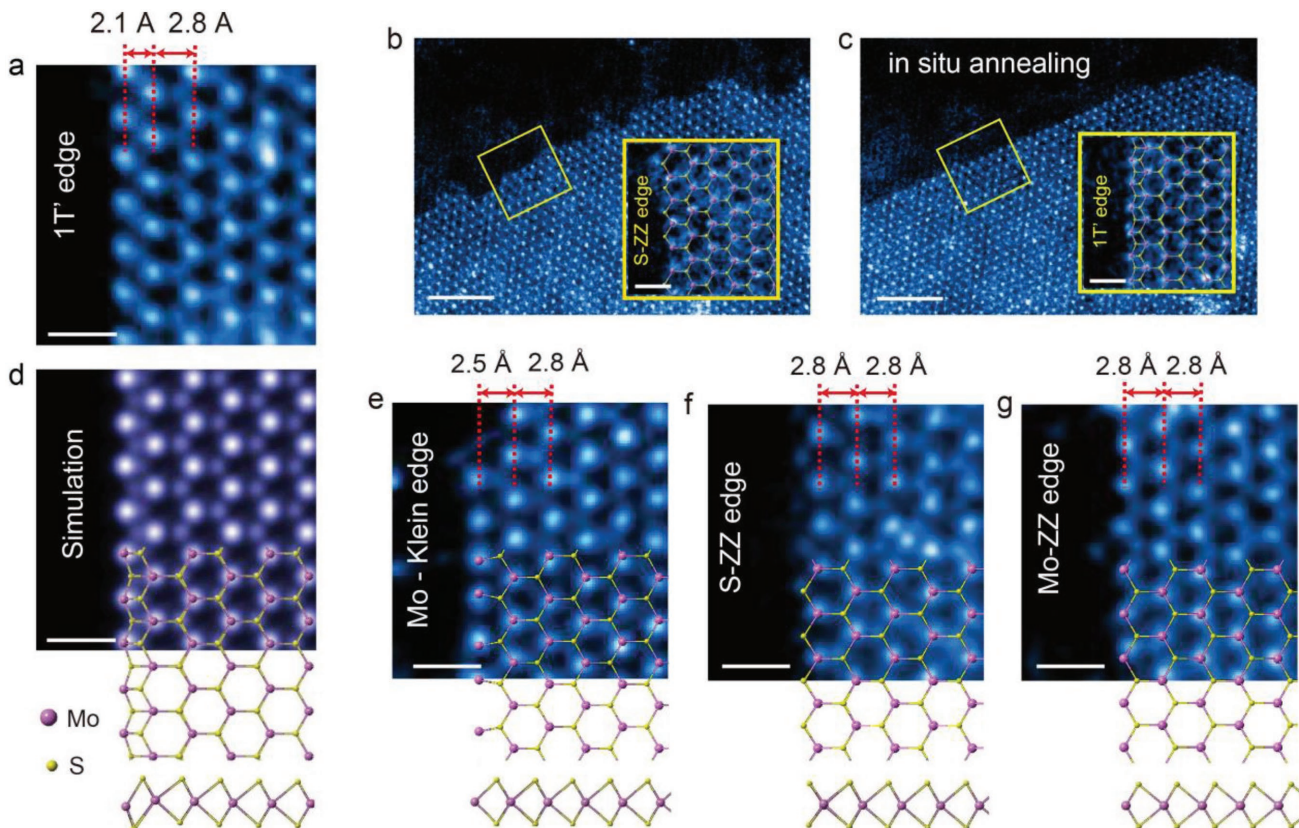


Figure 7. 1T'-edges in monolayer 1H-MoS₂ films. a) Atomic-resolution STEM-ADF image showing the atomically sharp 1T'-edges. STEM-ADF images of a region in the sample b) before and c) after in-situ annealing at 900 °C for 30 min inside the STEM. The S-ZZ edge from the region highlighted in (b) evolved into a 1T'-edge, as highlighted in the yellow box region in (c). d) Simulated image with overlaid DFT optimized 1T'-edges. e–g) Atomic-resolution STEM-ADF images showing the Mo-Klein (e), S-ZZ (f), and Mo-ZZ (g) edges. DFT optimized atomic models are overlaid and corresponding side views are depicted in the lower panels. Scale bars: 0.5 nm in (a,d–g) and insets of (b,c); 2 nm in (b,c). a–g) Adapted with permission.^[78] Copyright 2018, American Chemical Society.

However, various polymorphs can coexist in CVD-grown MoS₂ arising from multiple degrees of freedom in intralayer or interlayer stacking sequences. 1H polymorphs are sometimes misidentified as 1T in the STEM-ADF images due to scattering or image processing artifacts. We have discussed the protocols to avoid this here. Although the basal plane of monolayer MoS₂ usually adopts the 1H phase, it is noticed that edge or boundary discontinuities can manifest in a wide range of reconstructions. Correct identification of different phases provides insights on growth dynamics as well as structure–property correlations.

Acknowledgements

K.P.L. is grateful for the MOE Tier 2 grant “Porous, conjugated molecular framework for energy storage” (MOE2016-T2-1-003) and also funding by SinBeRISE CREATE, National Research Foundation, Prime Minister’s Office. S.J.P. is grateful for the MOE Tier 2 grant “Atomic scale understanding and optimization of defects in 2D materials” (MOE2017-T2-2-139) and to the National University of Singapore for funding.

Conflict of Interest

The authors declare no conflict of interest.

Keywords

atomic edges, molybdenum disulfide, phase engineering, phase identification, scanning transmission electron microscopy

Received: April 15, 2018

Revised: May 31, 2018

Published online:

- [1] K. F. Mak, C. Lee, J. Hone, J. Shan, T. F. Heinz, *Phys. Rev. Lett.* **2010**, *105*, 136805.
- [2] D. Fu, X. Zhao, Y.-Y. Zhang, L. Li, H. Xu, A.-R. Jang, S. I. Yoon, P. Song, S. M. Poh, T. Ren, Z. Ding, W. Fu, T. J. Shin, H. S. Shin, S. T. Pantelides, W. Zhou, K. P. Loh, *J. Am. Chem. Soc.* **2017**, *139*, 9392.
- [3] B. Radisavljevic, A. Radenovic, J. Brivio, V. Giacometti, A. Kis, *Nat. Nanotechnol.* **2011**, *6*, 147.
- [4] M. Kan, J. Y. Wang, X. W. Li, S. H. Zhang, Y. W. Li, Y. Kawazoe, Q. Sun, P. Jena, *J. Phys. Chem. C* **2014**, *118*, 1515.
- [5] M. Calandra, *Phys. Rev. B: Condens. Matter Mater. Phys.* **2013**, *88*, 245428.
- [6] K. Leng, Z. Chen, X. Zhao, W. Tang, B. Tian, C. T. Nai, W. Zhou, K. P. Loh, *ACS Nano* **2016**, *10*, 9208.
- [7] R. Kappera, D. Voiry, S. E. Yalcin, B. Branch, G. Gupta, A. D. Mohite, M. Chhowalla, *Nat. Mater.* **2014**, *13*, 1128.
- [8] M. Acerce, D. Voiry, M. Chhowalla, *Nat. Nanotechnol.* **2015**, *10*, 313.
- [9] M. Chhowalla, H. S. Shin, G. Eda, L. J. Li, K. P. Loh, H. Zhang, *Nat. Chem.* **2013**, *5*, 263.
- [10] D. Voiry, A. Mohite, M. Chhowalla, *Chem. Soc. Rev.* **2015**, *44*, 2702.
- [11] R. Suzuki, M. Sakano, Y. J. Zhang, R. Akashi, D. Morikawa, A. Harasawa, K. Yaji, K. Kuroda, K. Miyamoto, T. Okuda, K. Ishizaka, R. Arita, Y. Iwasa, *Nat. Nanotechnol.* **2014**, *9*, 611.
- [12] J. Chen, X. Zhao, G. Grinblat, Z. Chen, S. J. R. Tan, W. Fu, Z. Ding, I. Abdelwahab, Y. Li, D. Geng, Y. Liu, K. Leng, B. Liu, W. Liu, W. Tang, S. A. Maier, S. J. Pennycook, K. P. Loh, *Adv. Mater.* **2018**, *30*, 1704674.
- [13] L. Cai, J. He, Q. Liu, T. Yao, L. Chen, W. Yan, F. Hu, Y. Jiang, Y. Zhao, T. Hu, Z. Sun, S. Wei, *J. Am. Chem. Soc.* **2015**, *137*, 2622.
- [14] J. Jiang, Z. K. Liu, Y. Sun, H. F. Yang, C. R. Rajamathi, Y. P. Qi, L. X. Yang, C. Chen, H. Peng, C.-C. Hwang, S. Z. Sun, S.-K. Mo, I. Vobornik, J. Fujii, S. S. P. Parkin, C. Felser, B. H. Yan, Y. L. Chen, *Nat. Commun.* **2017**, *8*, 13973.
- [15] C. Guo, J. Pan, H. Li, T. Lin, P. Liu, C. Song, D. Wang, G. Mu, X. Lai, H. Zhang, W. Zhou, M. Chen, F. Huang, *J. Mater. Chem. C* **2017**, *5*, 10855.
- [16] O. L. Krivanek, M. F. Chisholm, V. Nicolosi, T. J. Pennycook, G. J. Corbin, N. Dellby, M. F. Murfitt, C. S. Own, Z. S. Szilagyi, M. P. Oxley, S. T. Pantelides, S. J. Pennycook, *Nature* **2010**, *464*, 571.
- [17] M. Lentzen, *Microsc. Microanal.* **2006**, *12*, 191.
- [18] J. Yan, J. Xia, X. Wang, L. Liu, J.-L. Kuo, B. K. Tay, S. Chen, W. Zhou, Z. Liu, Z. X. Shen, *Nano Lett.* **2015**, *15*, 8155.
- [19] M. Haider, H. Rose, S. Uhlemann, E. Schwan, B. Kabius, K. Urban, *Ultramicroscopy* **1998**, *75*, 53.
- [20] D. Xu, Y. Zhu, J. Liu, Y. Li, W. Peng, G. Zhang, F. Zhang, X. Fan, *Nanotechnology* **2016**, *27*, 385604.
- [21] J. M. Cowley, A. F. Moodie, *Acta Crystallogr.* **1957**, *10*, 609.
- [22] W. Coene, G. Janssen, M. Op De Beeck, D. Van Dyck, *Phys. Rev. Lett.* **1992**, *69*, 3743.
- [23] W. K. Hsieh, F. R. Chen, J. J. Kai, A. I. Kirkland, *Ultramicroscopy* **2004**, *98*, 99.
- [24] E. J. Kirkland, *Advanced Computing in Electron Microscopy*, Springer, New York **2010**.
- [25] J. Brivio, D. T. L. Alexander, A. Kis, *Nano Lett.* **2011**, *11*, 5148.
- [26] Z. Wang, S. Ning, T. Fujita, A. Hirata, M. Chen, *ACS Nano* **2016**, *10*, 10308.
- [27] U. Maitra, U. Gupta, M. De, R. Datta, A. Govindaraj, C. N. R. Rao, *Angew. Chem., Int. Ed.* **2013**, *52*, 13057.
- [28] S. J. Pennycook, P. D. Nellist, *Scanning Transmission Electron Microscopy*, Springer, New York **2011**.
- [29] P. D. Nellist, S. J. Pennycook, *J. Microsc.* **1998**, *190*, 159.
- [30] S. J. Pennycook, D. E. Jesson, *Ultramicroscopy* **1991**, *37*, 14.
- [31] S. J. Pennycook, *Ultramicroscopy* **1989**, *30*, 58.
- [32] A. Y. Borisevich, A. R. Lupini, S. J. Pennycook, *Proc. Natl. Acad. Sci. USA* **2006**, *103*, 3044.
- [33] Z. Wang, Y. Shen, Y. Ito, Y. Zhang, J. Du, T. Fujita, A. Hirata, Z. Tang, M. Chen, *ACS Nano* **2018**, *12*, 1571.
- [34] S. Yamashita, S. Koshiya, T. Nagai, J. Kikkawa, K. Ishizuka, K. Kimoto, *Microscopy* **2015**, *64*, 409.
- [35] Y.-C. Lin, D. O. Dumcenco, Y.-S. Huang, K. Suenaga, *Nat. Nanotechnol.* **2014**, *9*, 391.
- [36] A. Yan, W. Chen, C. Ophus, J. Ciston, Y. Lin, K. Persson, A. Zettl, *Phys. Rev. B* **2016**, *93*, 041420(R).
- [37] R. J. Toh, Z. Sofer, J. Luxa, D. Sedmidubský, M. Pumera, *Chem. Commun.* **2017**, *53*, 3054.
- [38] M. C. Scott, C. C. Chen, M. Mecklenburg, C. Zhu, R. Xu, P. Ercius, U. Dahmen, B. C. Regan, J. Miao, *Nature* **2012**, *483*, 444.
- [39] S. Ning, T. Fujita, A. Nie, Z. Wang, X. Xu, J. Chen, M. Chen, S. Yao, T. Y. Zhang, *Ultramicroscopy* **2018**, *184*, 274.
- [40] C. Tan, W. Zhao, A. Chaturvedi, Z. Fei, Z. Zeng, J. Chen, Y. Huang, P. Ercius, Z. Luo, X. Qi, B. Chen, Z. Lai, B. Li, X. Zhang, J. Yang, Y. Zong, C. Jin, H. Zheng, C. Kloc, H. Zhang, *Small* **2016**, *12*, 1866.
- [41] W. Chen, J. Gu, Q. Liu, R. Luo, L. Yao, B. Sun, W. Zhang, H. Su, B. Chen, P. Liu, D. Zhang, *ACS Nano* **2018**, *12*, 308.
- [42] P. D. Nellist, M. F. Chisholm, N. Dellby, O. L. Krivanek, M. F. Murfitt, Z. S. Szilagyi, A. R. Lupini, A. Borisevich, W. H. Sides, S. J. Pennycook, *Science* **2004**, *305*, 1741.

- [43] S. Luo, G. Hao, Y. Fan, L. Kou, C. He, X. Qi, C. Tang, J. Li, K. Huang, J. Zhong, *Nanotechnology* **2015**, 26, <https://doi.org/10.1088/0957-4484/26/10/105705>.
- [44] X. Zhao, Z. Ding, J. Chen, J. Dan, S. M. Poh, W. Fu, S. J. Pennycook, W. Zhou, K. P. Loh, *ACS Nano* **2018**, 12, 1940.
- [45] X. Zhao, J. Kotakoski, J. C. Meyer, E. Sutter, P. Sutter, A. V. Krasheninnikov, U. Kaiser, W. Zhou, *MRS Bull.* **2017**, 42, 667.
- [46] H. P. Komsa, S. Kurasch, O. Lehtinen, U. Kaiser, A. V. Krasheninnikov, *Phys. Rev. B: Condens. Matter Mater. Phys.* **2013**, 88, 035301.
- [47] C. Tan, Z. Luo, A. Chaturvedi, Y. Cai, Y. Du, Y. Gong, Y. Huang, Z. Lai, X. Zhang, L. Zheng, X. Qi, M. H. Goh, J. Wang, S. Han, X. J. Wu, L. Gu, C. Kloc, H. Zhang, *Adv. Mater.* **2018**, 30, 1705509.
- [48] S. S. Chou, N. Sai, P. Lu, E. N. Coker, S. Liu, K. Artyushkova, T. S. Luk, B. Kaehr, C. J. Brinker, *Nat. Commun.* **2015**, 6, 8311.
- [49] X.-B. Li, Y.-J. Gao, H.-L. Wu, Y. Wang, Q. Guo, M.-Y. Huang, B. Chen, C.-H. Tung, L.-Z. Wu, *Chem. Commun.* **2017**, 53, 5606.
- [50] Y. Yin, J. Han, Y. Zhang, X. Zhang, P. Xu, Q. Yuan, L. Samad, X. Wang, Y. Wang, Z. Zhang, P. Zhang, X. Cao, B. Song, S. Jin, *J. Am. Chem. Soc.* **2016**, 138, 7965.
- [51] J.-M. Zuo, A. B. Shah, H. Kim, Y. Meng, W. Gao, J.-L. Rouviére, *Ultramicroscopy* **2013**, 136, 50.
- [52] W. V. Nicholson, R. M. Glaeser, *J. Struct. Biol.* **2001**, 133, 90.
- [53] X. Zhao, Z. Ding, J. Chen, J. Dan, S. M. Poh, W. Fu, S. J. Pennycook, W. Zhou, K. P. Loh, *ACS Nano* **2018**, 12, 1940.
- [54] Y. H. Lee, X. Q. Zhang, W. Zhang, M. T. Chang, C. T. Lin, K. D. Chang, Y. C. Yu, J. T. Wang, C. S. Chang, L. J. Li, T. W. Lin, *Adv. Mater.* **2012**, 24, 2320.
- [55] J. Chen, W. Tang, B. Tian, B. Liu, X. Zhao, Y. Liu, T. Ren, W. Liu, D. Geng, H. Y. Jeong, H. S. Shin, W. Zhou, K. P. Loh, *Adv. Sci.* **2016**, 31, 1500033.
- [56] J. Shi, P. Yu, F. Liu, P. He, R. Wang, L. Qin, J. Zhou, X. Li, J. Zhou, X. Sui, S. Zhang, Y. Zhang, Q. Zhang, T. C. Sum, X. Qiu, Z. Liu, X. Liu, *Adv. Mater.* **2017**, 29, 1701486.
- [57] T. Jiang, H. Liu, D. Huang, S. Zhang, Y. Li, X. Gong, Y.-R. Shen, W.-T. Liu, S. Wu, *Nat. Nanotechnol.* **2014**, 9, 825.
- [58] Y. Zhang, Q. Ji, G. F. Han, J. Ju, J. Shi, D. Ma, J. Sun, Y. Zhang, M. Li, X. Y. Lang, Y. Zhang, Z. Liu, *ACS Nano* **2014**, 8, 8617.
- [59] A. Yan, C. S. Ong, D. Y. Qiu, C. Ophus, J. Ciston, C. Merino, S. G. Louie, A. Zettl, *J. Phys. Chem. C* **2017**, 121, 22559.
- [60] J. Suh, T. L. Tan, W. Zhao, J. Park, D.-Y. Lin, T.-E. Park, J. Kim, C. Jin, N. Saigal, S. Ghosh, Z. M. Wong, Y. Chen, F. Wang, W. Walukiewicz, G. Eda, J. Wu, *Nat. Commun.* **2018**, 9, 199.
- [61] N. Cortés, L. Rosales, P. A. Orellana, A. Ayuela, J. W. González, *Sci. Rep.* **2018**, 8, 2143.
- [62] Z. Wang, P. Liu, Y. Ito, S. Ning, Y. Tan, T. Fujiita, A. Hirata, M. Chen, *Sci. Rep.* **2016**, 6, 21536.
- [63] K. Chang, X. Hai, H. Pang, H. Zhang, L. Shi, G. Liu, H. Liu, G. Zhao, M. Li, J. Ye, *Adv. Mater.* **2016**, 28, 10033.
- [64] J. Heising, M. G. Kanatzidis, *J. Am. Chem. Soc.* **1999**, 121, 638.
- [65] Q. Liu, X. Li, Q. He, A. Khalil, D. Liu, T. Xiang, X. Wu, L. Song, *Small* **2015**, 11, 5556.
- [66] C.-H. Ho, W.-H. Chen, K. K. Tiong, K.-Y. Lee, A. Gloter, A. Zobelli, O. Stephan, L. H. G. Tizei, *ACS Nano* **2017**, 11, 11162.
- [67] Y. Li, K. A. N. Duerloo, K. Wauson, E. J. Reed, *Nat. Commun.* **2016**, 7, 10671.
- [68] X. Qian, J. Liu, L. Fu, J. Li, *Science* **2014**, 346, 1344.
- [69] S. N. Shirodkar, U. V. Waghmare, *Phys. Rev. Lett.* **2014**, 112, 157601.
- [70] X. B. Chen, Z. L. Chen, J. Li, *Chin. Sci. Bull.* **2013**, 58, 1632.
- [71] S. J. R. Tan, I. Abdelwahab, Z. Ding, X. Zhao, T. Yang, G. Z. J. Loke, H. Lin, I. Verzhbitskiy, S. M. Poh, H. Xu, C. T. Nai, W. Zhou, G. Eda, B. Jia, K. P. Loh, *J. Am. Chem. Soc.* **2017**, 139, 2504.
- [72] K. K. Amara, Y. Chen, Y. C. Lin, R. Kumar, E. Okunishi, K. Suenaga, S. Y. Quek, G. Eda, *Chem. Mater.* **2016**, 28, 2308.
- [73] F. Wypych, R. Schöllhorn, *J. Chem. Soc., Chem. Commun.* **1992**, 1386.
- [74] F. Wypych, C. Solenthaler, R. Prins, T. Weber, *J. Solid State Chem.* **1999**, 144, 430.
- [75] F. Wypych, T. Weber, R. Prins, *Surf. Sci.* **1997**, 380, L474.
- [76] F. Wypych, T. Weber, R. Prins, *Chem. Mater.* **1998**, 10, 723.
- [77] Y. Yu, G.-H. Nam, Q. He, X.-J. Wu, K. Zhang, Z. Yang, J. Chen, Q. Ma, M. Zhao, Z. Liu, F.-R. Ran, X. Wang, H. Li, X. Huang, B. Li, Q. Xiong, Q. Zhang, Z. Liu, L. Gu, Y. Du, W. Huang, H. Zhang, *Nat. Chem.* **2018**, 10, 638.
- [78] X. Zhao, D. Fu, Z. Ding, Y. Y. Zhang, D. Wan, S. J. R. Tan, Z. Chen, K. Leng, J. Dan, W. Fu, D. Geng, P. Song, Y. Du, T. Venkatesan, S. T. Pantelides, S. J. Pennycook, W. Zhou, K. P. Loh, *Nano Lett.* **2018**, 18, 482.
- [79] D. Zhu, H. Shu, F. Jiang, D. Lv, V. Asokan, O. Omar, J. Yuan, Z. Zhang, C. Jin, *NPJ 2D Mater. Appl.* **2017**, 1, 8.